Intrinsic $LiNbO_3$ point defects from hybrid density functional calculations

Yanlu Li,* W. G. Schmidt, and S. Sanna
Lehrstuhl für Theoretische Physik, Universität Paderborn, 33095 Paderborn, Germany
(Received 13 November 2013; revised manuscript received 18 February 2014; published 31 March 2014)

The formation energies and charge transition levels of the most relevant $LiNbO_3$ intrinsic point defects, i.e., Nb antisites and Li as well Nb vacancies, are studied from *first principles*. Thereby isolated defects are modeled in the framework of the density functional theory with local and hybrid exchange-correlation functionals. The inclusion of nonlocal exchange opens the $LiNbO_3$ fundamental band gap by nearly 2 eV and modifies considerably the relative stability of the investigated defects with respect to values calculated with local functionals. On the other hand, supercell symmetry and finite-size errors in calculations using periodic boundary conditions are found to have a major influence on the outcome of the simulations. It is found that, in particular, the Nb vacancy causes a long-range strain field and requires very large supercells for its adequate modeling. Compared to previous theoretical results we find an enhanced stability of the Nb vacancy with respect to the other defects. The V_{Nb}^{-5} is predicted to be stable for Fermi level positions in the upper part of the band gap.

DOI: 10.1103/PhysRevB.89.094111 PACS number(s): 61.72.J−, 61.66.Fn

I. INTRODUCTION

Lithium niobate ($LiNbO_3$; LN) is a versatile material, due to its ferroelectric, piezoelectric, photorefractive, and electro-optical properties, that is widely used for optical waveguides, piezoelectric sensors, optical modulators, and various other linear and nonlinear optical applications [1,2]. Numerous investigations of the structure and chemical composition of LN have revealed a high degree of ionic disorder and Li_2O deficiency in most LN crystals [3,4]. Many LN physical properties, such as the refractive index, the photorefractivity, the birefringence, the linear electro-optical effect, and the Curie temperature [3,5–8], depend, to a large extent, on intrinsic defects. Understanding the defect properties is therefore of key importance for many LN applications, as pointed out in the recent review by Schirmer *et al*. [9].

Several experiments [10–12] have excluded the presence of oxygen vacancies in LN but revealed the presence of a large amount of Nb antisite (Nb_{Li}) defects instead. They might be charge compensated either by Nb vacancies (V_{Nb}) in the so-called Nb vacancy model [11] or by Li vacancies (V_{Li}) in the Li vacancy model [13]. Theory has played an important role in characterizing the interplay of defects and impurities in LN. Donnerberg *et al*. [14] pointed out that the formation of niobium vacancies to compensate for the niobium antisites is energetically less favorable than the formation of lithium vacancies. Nahm and Park investigated the microscopic properties of the Nb_{Li} antisite by local-density approximation (LDA) plus Hubbard-U electronic structure calculations (LDA + U) [15], providing strong theoretical support for the polaron model proposed by Schirmer *et al*. [9]. A recent first-principles work by Xu *et al*. [16] showed that the cluster consisting of a niobium antisite compensated by lithium vacancies is most stable under Nb_2O_5-rich conditions, and the Li-Frenkel defects had the lowest formation energy for Li_2O-rich conditions. However, Wilkinson *et al*. [17] suggested that the degree of filling of the Li sites by Nb ions is accidental and may depend on the growth conditions, so one may expect the coexistence of all three defects—Nb_{Li}, V_{Li}, and V_{Nb}—in as-grown Li-deficient crystals. Unfortunately, the picture that arises from the calculations available is not fully conclusive. While the two *ab initio* studies that have been performed on intrinsic LN point defects [16,18] conclude that the lithium-vacancy model is the most probable LN defect model, there is appreciable scatter in the reported defect formation energies (DFEs) and charge transition levels (CTLs). The former differ by several electron volts, and different charge states are reported. The Nb vacancy, for example, is reported to be neutral for Fermi energies in the lower part of the band gap in Ref. [16], while it is threefold negatively charged according to Ref. [18]. The striking differences between results obtained within similar approaches are due to the fact that the calculation of DFEs and CTLs is a very challenging task.

On the one hand, the modeling of point defects within the density functional theory (DFT) typically rests on periodic boundary conditions (PBCs) and is thus plagued by problems due to the interaction of the defect with its periodic images [19–24]. This results in calculated DFEs and CTLs that strongly depend on the size and geometry of the supercell. Li *et al*. [18], e.g., calculate V_{Nb}^{-5} formation energies of −114 and 13 eV using supercells containing 80 and 180 atoms, respectively. Obviously, the problem is particularly severe for charged defects and several schemes have been suggested in order to correct for the spurious interaction between defects modeled within PBC [21–24].

On the other hand, the commonly used LDA and the generalized gradient approximation (GGA) to DFT systematically underestimate the band gaps of semiconductors and insulators [25]. This so-called *band-gap problem* of the LDA and GGA severely affects the predictive power of these approximations when applied to defect levels (see, e.g., Refs. [26] and [27]. Spurious effects due to local functionals for the description of electron exchange and correlation (XC) are particularly severe in cases of strong correlations such as occurring in the highly localized Nb d states. Moreover, LDA and GGA suffer from the self-interaction error, which can affect the position of defect levels with respect to the band edges.

*yanlu.li@upb.de

While at first glance the DFT-LDA band gap of 3.48 eV calculated for ferroelectric LN [28] is comparatively close to the frequently cited experimental value of 3.78 eV [29], closer inspection shows that apparent agreement is caused by the high exciton binding energy in LN, which results in a strong deviation between the optical and the transport gap [30]. In fact, quasiparticle corrections calculated within the GW approximation blue-shift the DFT single-particle excitation energies by about 2 eV, and, if used as input for the Bethe-Salpeter equation, result in an excellent reproduction of the measured LN optical response [8]. Unfortunately, GW calculations are too time-consuming to be applied to large supercells as required for the calculation of point defects. Hybrid DFT calculations, where the XC functionals contain some amount of exact exchange from Hartree-Fock theory, such as proposed, e.g., by Heyd *et al*. [31,32], present a viable alternative. Indeed, this approach has been demonstrated to result in a reliable description of DFEs and defect levels in wide-band-gap semiconductors [33–40].

In the present work the energetics and electronic properties of the most relevant intrinsic LN point defects Nb_{Li}, V_{Li}, and V_{Nb} are studied within DFT with a hybrid XC functional. In order to properly tackle the two main (yet essentially unrelated) issues affecting the calculation of the DFEs, namely, the finite-size problem due to the supercell method and the poor description of the electronic structure in DFT-GGA, we employ a two-step approach. In the first step, we perform local and hybrid DFT calculations for 120-atom supercells, in order to estimate the hybrid-functional correction to classically calculated DFEs. In the second step, large supercells, containing up to 480 atoms, are used to calculate the DFEs within local DFT. The results obtained for various supercell sizes are extrapolated to infinite cell dimensions, and the previously calculated hybrid-functional corrections added to the DFEs. In this way we model the electronic structure of the point defects at the hybrid-functional level of accuracy, without suffering from the limited cell size in the calculation of the DFEs.

II. METHODOLOGY

A. Computational details

The present calculations employ the Vienna *ab initio* Simulation Package (VASP) [41,42] implementation of DFT in conjunction with the projector-augmented-wave (PAW) formalism [43]. Thereby the Li $2s^1$, Nb $4p^6 5s^1 4d^4$, and O $2s^2 2p^4$ states are treated as valence electrons. The electronic wave functions are expanded in plane waves using an energy cutoff of 400 eV. Isolated Nb antisites Nb_{Li}, Li vacancies V_{Li}, and Nb vacancies V_{Nb} as shown in Fig. 1 are modeled with cells of different sizes.

Rhombohedral supercells containing 80 and 360 atoms, as well as hexagonal supercells containing 120, 240, 270, 360, and 480 atoms, are used for the defect calculations within the DFT-GGA. Thereby the Perdew-Burke-Ernzerhof functional (PBE) [44] is used to model the electron XC energy within the GGA. Structural relaxation is performed using 0.01 eV/Å as the force convergence criterion. Apart from the largest hexagonal supercells, where only the Γ point is used, a $4 \times 4 \times 4$ Monkhorst-Pack mesh [45] is employed to sample the Brillouin zone.

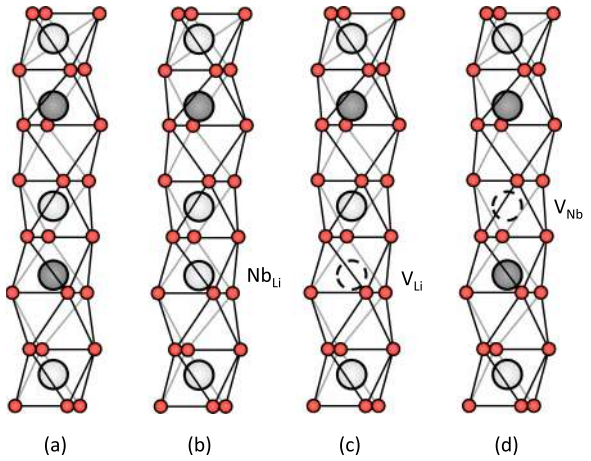

FIG. 1. (Color online) Ball-and-stick models for defect-free LN (a) and material with Nb_{Li} (b), V_{Li} (c), and V_{Nb} (d) point defects. O, small circles; Li, large dark circles; Nb atoms, large light circles.

Smaller hexagonal supercells containing 120 atoms are used for the hybrid-functional calculations, instead. Thereby the electron exchange and correlation energy is modeled with the Hyde-Scuseria-Ernzerhof (HSE06) screened hybrid functional [31,32]. The short-range component of the exchange functional contains 25% Hartree-Fock exchange complementing the PBE-type XC description. A $2 \times 2 \times 2$ Monkhorst-Pack mesh [45] is employed to sample the Brillouin zone.

B. Formation energies and chemical potentials

We calculate the DFE for the charge state q dependent on the Fermi level position according to [23,46]

$$E_f(X^q) = E^{\text{total}}(X^q) - E^{\text{total}}(\text{bulk}) + \sum_i n_i \mu_i + q(E_F + E_v + \Delta V), \quad (1)$$

where $E^{\text{total}}(X^q)$ is the total energy derived from a supercell with defect X, $E^{\text{total}}(\text{bulk})$ is the total energy of the defect-free supercell, n_i indicates the number of atoms of species i that have been added or removed upon defect creation, and μ_i are the corresponding chemical potentials. E_F is the Fermi level with respect to the bulk valence-band maximum E_v, and ΔV is a correction term which aligns the reference potential in our defect supercell with that in the bulk [46]. The chemical potentials μ_i depend on the preparation conditions. As shown, e.g., by Phillpot and co-workers [16], thermodynamic considerations restrict the accessible range of the μ_i if one requires the LN stability: Let us define $\Delta\mu_{Li}$, $\Delta\mu_{Nb}$, and $\Delta\mu_O$ as differences from the respective bulk values of the chemical potential of Li, Nb, and O. These are calculated using O_2 and the body-centered cubic structures (space group $Im\bar{3}m$) of metallic Li and Nb as reference phases, with the computational parameters described in Ref. [47]. The stability of the ternary compound LN against decomposition into its single components constraints the $\Delta\mu_i$ to negative values. Furthermore, the stoichiometric sum of the $\Delta\mu_i$ has to equal

the LN formation enthalpy,

$$\Delta\mu_{\mathrm{Li}} + \Delta\mu_{\mathrm{Nb}} + 3\Delta\mu_{\mathrm{O}} = -\Delta H_f^{\mathrm{LN}}. \quad (2)$$

The thermodynamically stable region is between the two extremes of LN being in equilibrium with niobium oxide and lithium oxide, respectively [16,47]. They are described by the relations

$$2\Delta\mu_{\mathrm{Li}} + \Delta\mu_{\mathrm{O}} = -\Delta H_f^{\mathrm{Li_2O}} \quad \text{and} \quad (3)$$

$$2\Delta\mu_{\mathrm{Nb}} + 5\Delta\mu_{\mathrm{O}} = -\Delta H_f^{\mathrm{Nb_2O_5}}. \quad (4)$$

These requirements are visualized in Fig. 2 (see also Fig. 6 in Ref. [47] for an alternative, three-dimensional representation). Within the triangle ADG the stoichiometric sum of $\Delta\mu_{\mathrm{Li}}$, $\Delta\mu_{\mathrm{Nb}}$, and $\Delta\mu_{\mathrm{O}}$ yields the LN formation enthalpy, i.e., Eq. (2). Equation (3) defines the region within the triangle BDF, while the region enclosed between points A, C, E, and G satisfies Eq. (4). The shaded overlap region indicates the LN stability range. Values of the chemical potentials outside this region lead to the precipitation of other phases. Here we model the point defects using Nb-rich conditions (line CE), since even nearly stoichiometric LN crystals are still Li deficient. Thus, the chemical potentials of Li and Nb used here are −4.37 and −20.19 eV, respectively. A different choice of the reference state will modify the relative stability of the investigated defects. Strictly speaking, the Gibbs free energy of formation has to be used to determine the chemical potentials instead of the Helmholtz enthalpy in Eqs. (2) to (4). However, it is customary to replace $G(p,T)$ with the Helmholtz enthalpy, as the entropic terms are expected to be of the same order of magnitude for all the investigated systems, as explained in some detail in Ref. [16] (and references therein). Neglecting the entropy term will thus not qualitatively change our conclusions.

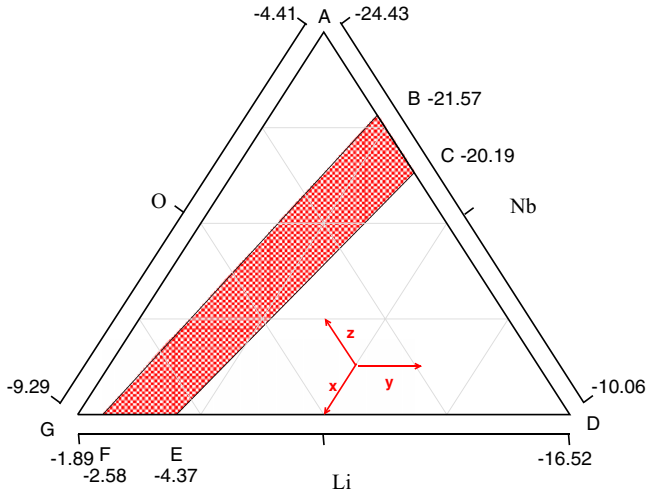

FIG. 2. (Color online) Stability range of the chemical potentials (in eV) of the $LiNbO_3$ constituents. The region enclosed between points B, D, and F satisfies Eq. (3), while the region enclosed between points A, C, E, and G satisfies Eq. (4). The shaded region is the intersection between them and represents the thermodynamically allowed range of the chemical potentials.

C. Finite-size errors

The general concept of finite-size error includes error sources of different natures that arise from the limited size of the supercell within PBCs. This term is made up of two main contributions, namely, the electrostatic interaction between charged defects in neighboring cell images and the structural strain introduced by the defect. In strongly piezoelectric materials such as $LiNbO_3$, where a localized charge generates a sizable lattice distortion, the two contributions are deeply merged.

The electrostatic energy of neutral aperiodic systems converges as $\mathcal{O}(L^{-5})$ in calculations using PBCs [22], where L is the linear dimension of the supercell. For charged systems, convergence at this rate can be achieved by the addition of correction terms as suggested by Makov and Payne [22]. Assuming an essentially point-like charge distribution of the excess defect charge, the electrostatic energy can be expressed in a multipole expansion [22,49],

$$E^{\infty} = E_0 + \frac{q^2\alpha_M}{2\varepsilon_s L} + \frac{2\pi q Q}{3L^3\varepsilon_s} + \mathcal{O}(L^{-5}), \quad (5)$$

where E_0 is the calculated total energy of the system, q is the total charge, Q is the quadrupole moment of the defect-induced charge, α_M is the geometry-dependent Madelung constant, and ε_s is the static bulk dielectric constant. The application of such a correction for the calculation of DFE indeed works well for cases that are characterized by strongly localized excess charges [20,23,24].

Here we apply this scheme and thereby use the weighted average of the experimental values of the static dielectric tensor components $\varepsilon_s^{11} = 84$ and $\varepsilon_s^{33} = 29$ given in Ref. [50]. However, only corrections as given by the monopole are considered. This term is the Madelung energy of a lattice of point charges immersed in neutalizing jellium [21] and represents the spurious Coulomb interaction between charged defects due to the use of PBCs. We neglect the quadrupole term, as it is about one order of magnitude smaller than the Madelung energy for all investigated defects. This is due to the large supercells used in this work and the large dielectric constant of $LiNbO_3$. As an example, calculating the corrections for the dominant defect in congruent LN (i.e., the $\mathrm{Nb_{Li}^{+4}}$ antisite) in a 360-atom supercell ($L^3 = 3816.8$ Å^3) results in a Madelung energy of 0.340 eV and a quadrupole term of only 0.038 eV.

In addition, we linearly extrapolate the formation energies calculated for various cell sizes to infinite cell dimensions using a fitting procedure with weighting factors which are proportional to the number of atoms in the supercell, in order to account for the accuracy increase for larger supercells. In contrast to the Madelung correction, this approach addresses the defect-defect interaction due to strain fields in addition to the electrostatic interaction between the defect and its images.

III. RESULTS

As explained in Sec. I, modeling point defects in the framework of the DFT within the supercell approach are affected both by finite-size issues and by the poor electronic structure predicted with local XC potentials. The two effects

TABLE I. Summary of the bulk properties of ferroelectric $LiNbO_3$ calculated with a local and a hybrid potential. The rhombohedral lattice parameters a_R and α and the positions of the valence-band maximum (VBM) and of the conduction-band minimum (CBM) are listed, as well as the direct and indirect transition energy gaps.

	PBE	HSE06	Ref.
a_R	5.58 Å	5.55 Å	Exp. [48], 5.50 Å
α	55.71°	55.87°	Exp. [48], 55.52°
VBM	Γ	Γ	GW [8], Γ
CBM	Γ-K	Γ-A	GW [8], Γ-A
Indirect	3.37 eV	5.21 eV	GW [8], 5.36 eV
Direct	3.38 eV	5.28 eV	GW [8], 5.42 eV

have a different origin and are examined separately in this work. In the first step we address the differences in $LiNbO_3$ bulk properties and in the DFEs as calculated with local and hybrid DFT. In the second step we estimate the finite-size error within DFT-GGA. Finally, DFEs are calculated which take in account both the hybrid functional description of the electronic structure and the finite-size error due to the supercell approach within PBCs.

A. Estimation of the XC-induced error

The approximation of the electron XC by a (semi)local functional within DFT causes inaccuracies in the description of the electronic structure, leading to the well-known band gap problem of DFT. The application of hybrid potentials drastically improves the description of the LN electronic structure. Table I summarizes some of the bulk properties of ferroelectric $LiNbO_3$ calculated within the different approaches. Figure 3 represents the corresponding calculated electronic band structure. While the structural properties are rather similar, the application of hybrid potentials leads to a band-gap opening of 1.84 eV with respect to the value calculated within standard DFT. The value of 5.21 eV calculated with the hybrid functional is in very good agreement with the value of 5.36 eV calculated within the GW approximation [8]. The electronic band gap is indirect both within DFT-PBE and within DFT-HSE. However, while the conduction-band minimum (CBM) is placed between the Γ and the K point in DFT-PBE, it is placed between the Γ and the A point in DFT-HSE. However, within both DFT-PBE and hybrid-DFT, we find the lowest conduction band to be very flat around Γ. Therefore, the material can be regarded as having approximately a direct band gap at the Γ point.

Besides correcting the electronic band gap, hybrid functionals are expected to improve the description of strong correlations such as occur in the Nb *d* states and partially correct for the electronic self-interaction, which can result in a wrong alignment of the defect levels with respect to the band edges. Indeed, calculating the DFEs with hybrid DFT leads to pronounced energy changes—-up to several electron volts—with respect to DFEs calculated within DFT-PBE. This is shown in Fig. 4, where the DFE differences between HSE and PBE are shown for Nb_{Li}, V_{Li}, and V_{Nb} dependent on the charge state. It can be seen that HSE lowers the DFEs of Nb_{Li} with respect to PBE, while it increases the DFEs of V_{Li} and V_{Nb}. The latter shows the largest deviation. As we show later, this defect causes a pronouced lattice relaxation and a major rearrangement both in occupied and in conduction band states, which are more influenced by the nonlocal potentials. The deviation between PBE and HSE energies increases with the (absolute) charge state, suggesting that electronic self-interaction plays a major role. The deviations are most pronounced for Nb-related defects, i.e., the Nb antisite and Nb vacancy. This indicates that the strongly localized Nb *d* states are poorly described by the semilocal XC functional. Assuming that the error made by using a semilocal XC functional is primarily related to the orbital character of the defect-induced electronic states and their energy position rather than the size of the supercell, the definition of a nonlocal exchange correction of DFEs (XC) as the difference in the DFEs calculated within HSE versus PBE using the same

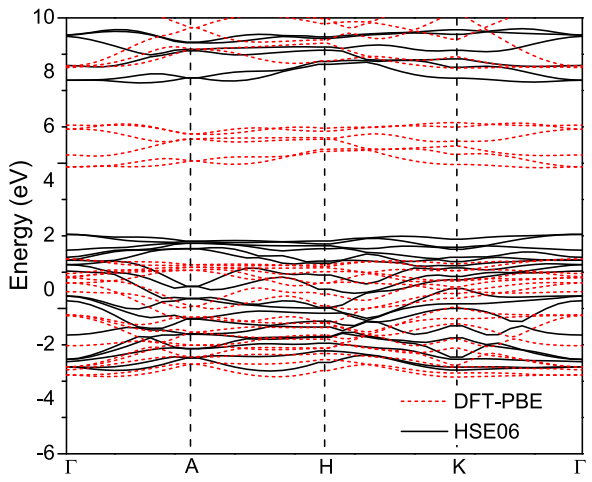

FIG. 3. (Color online) Electronic band structure of ferroelectric $LiNbO_3$ calculated with DFT-PBE (dashed lines) and hybrid DFT (straight lines). Application of the hybrid potential leads to a band-gap opening of 1.84 eV.

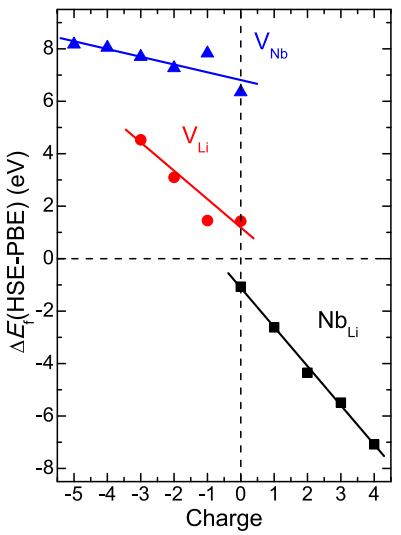

FIG. 4. (Color online) Defect formation energy difference between HSE and PBE (at Fermi energy $E_F = 0$) of Nb_{Li}, V_{Li}, and V_{Nb} in LN as a function of the charge state.

120-atom supercell (as in Fig. 4) is meaningful. This allows for estimation of the error made by finite supercells within PBCs in addition to the XC-related error. As we show in the following section, the influence of the PBCs can be corrected for by extrapolating the DFEs to infinite dimension. Such an extrapolation procedure, however, cannot be applied directly to the HSE calculations due to their far larger computational expense. Instead, we will perform it within DFT-PBE.

B. Estimation of the finite-size error

It is found that even DFEs calculated with a rather large supercell, containing 240 atoms, are not converged with respect to the cell size. Indeed, DFEs and CTLs modeled with cells of different size and geometries lead to different results, both concerning the relative defect stability and the succession of the charge states. The discrepancies are particularly severe in the case of the Nb vacancy. In this case deviations of several electron volts are found, even for supercells larger than 270 atoms. The sensitivity of the V_{Nb} results with respect to the application of PBCs confirms earlier findings [16,18]. We remark that not only the size of the supercell, but also its symmetry is important for a correct description of defect properties [51]. LN is polarized along the z direction, which is also the threefold rotation axis that characterizes the C_3 symmetry of the defects studied here. In order not to lift this symmetry due to PBCs, only hexagonal cells have been used. In fact, defects modeled within nonisotropic repetitions of the rhombohedral unit cell show pronounced differences with respect to the sequence of the CTLs, with a tendency for larger charge jumps.

Using hexagonal unit cells only, the DFEs calculated within DFT-PBE are extrapolated to infinite unit cell size. Thereby also the influence of the Madelung correction is probed. This is illustrated excellently in Fig. 5 for Nb_{Li}^{+4}, V_{Li}^{-1}, and V_{Nb}^{-1}. As expected, the Madelung correction reduces the dependence of the calculated formation energy from the cell size, for all considered defects. Accordingly, the correction decreases the slope of the DFEs in Fig. 5. For the most strongly charged defect investigated, V_{Nb}^{-5}, the influence of the Madelung correction on the extrapolated value is about 0.5 eV. However, since this correction is itself an approximation and the object of many discussions, we present in the following DFEs obtained by extrapolating the data calculated without applying this scheme (blue lines in Fig. 5).

The Nb_{Li} and V_{Li} energies calculated using 120-, 240-, and 360-atom cells show a roughly linear behavior that can well be extrapolated to infinite cell dimensions. This is not the case for V_{Nb}, which is much more sensitive to the finite-size effect. The fact that the Madelung correction only marginally modifies the DFEs indicates that long-range strain fields are the dominant source of error for the V_{Nb} calculations. In order to probe this presumption we investigate the dependence of the atomic relaxations around the defect on the supercell size. Calculations in very large, 540-atom, hexagonal supercells show atomic displacements larger than 0.01 Å within a radius of about 6 Å in the case of Nb_{Li} and V_{Li} and within a radius of about 11 Å in the case of V_{Nb}. Thus, while Nb_{Li} and V_{Li} defects might be calculated in a nearly strain-free 240-atom cell, the realistic description of the atomic displacements around V_{Nb} clearly requires supercells that contain more than 240 atoms. Therefore, calculations in 480-, 360-, and 270-atom cells were used to extrapolate the V_{Nb} defect energies.

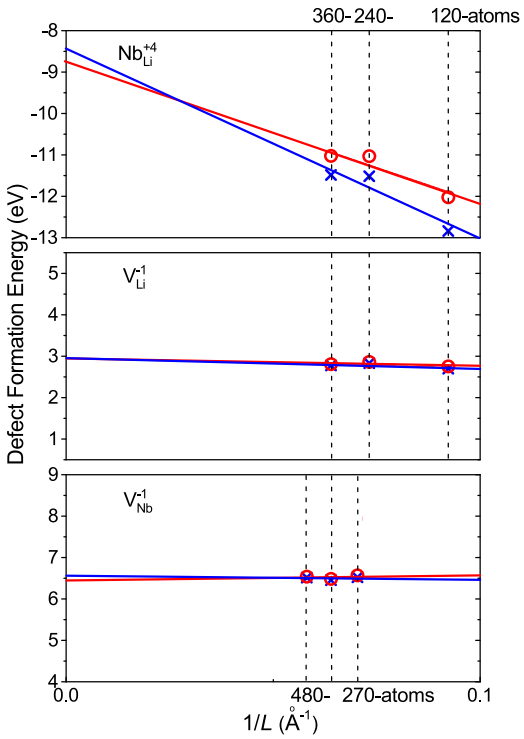

FIG. 5. (Color online) Defect formation energies of Nb_{Li}^{+4}, V_{Li}^{-1}, and V_{Nb}^{-1} calculated in hexagonal cells. Lines represent the linear fit of the calculated points. The effect of the Madelung correction (in red) is indicated.

C. Defect formation energies

If one assumes that the artifacts related to the PBCs discussed in the previous section, which are mainly due to spurious electrostatic and strain interactions between the defect and its images, are largely independent of the corrections needed to account for the use of a semilocal XC functional, one may calculate DFEs that approximately include both effects by adding the previously defined XC correction to the extrapolated PBE results. The results (denoted PBE + XC) are shown in Fig. 6 (straight lines) in comparison with the values obtained within HSE and PBE. It is seen that the PBE + XC results favor the Nb antisite Nb_{Li}^{+4} for values of the electron chemical potential in the lower third of the band gap, while the Li vacancy V_{Li}^{-1} is most favored for the electron chemical potential in midgap position. At Fermi level energies in the upper part of the band gap, the Nb vacancy V_{Nb}^{-5} is the most favored isolated point defect. Compared to the PBE results, the stability of Nb_{Li}^{+4} is drastically enhanced, while the stability of V_{Nb}^{-5} is slightly decreased. The Li vacancy V_{Li}^{-1} is more stable than V_{Nb}^{-5} in PBE + XC for Fermi energies in the midgap position, whereas these two defects have almost the same DFEs in PBE. The PBE + XC results thus support the experimental observations [52,53] that Nb antisites and Li vacancies are dominant in congruent LN. Our data also indicate that in some specific cases, where the Fermi energy

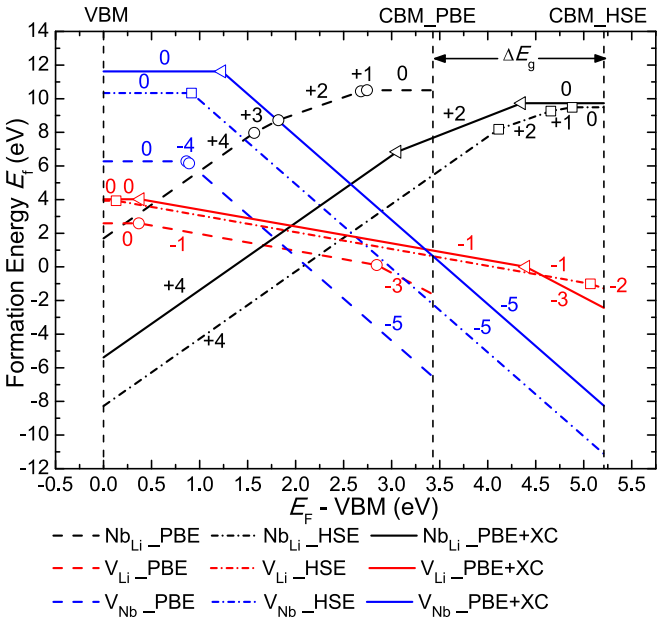

FIG. 6. (Color online) Defect formation energies within PBE, HSE, and PBE + XC of Nb_{Li}, V_{Li}, and V_{Nb} in LN as a function of the Fermi energy.

is in the upper part of the electronic band gap, the Nb vacancy model describes the LN defect structure. This agrees with recent LN optical response calculations [8], where the assumption of the Nb vacancy model was found to improve the comparison between the simulated spectra and the measurements for congruent samples. However, in the majority of LN samples the Fermi energy lies in the lower part of the fundamental band gap.

The HSE calculations not only affect the relative stability of the isolated point defects, but also modify the calculated CTLs. The Nb antisite +1 and +3 states as well as the −4 state of V_{Nb} are unstable in PBE + XC. For Fermi level positions in the upper half of the band gap, the Nb antisite shows a negative-U behavior and accepts two additional electrons simultaneously. Comparing the HSE and PBE + XC results, it can be seen that the correction of the finite-size error mainly leads to two changes: The Nb antisite +1 state, which is stable within the HSE in a very narrow range of electron chemical potentials close to the CBM, is not observed in the PBE + XC, and the Li vacancy, which is close to the CBM, is charged −2 in the HSE and −3 in the PBE + XC. Since these modifications are restricted to a small range of the Fermi level position close to the CBM and because Nb_{Li}^{+1} and V_{Li}^{-2} are far lower in energy there, they are not likely to have actual implications for the LN defect structure. In the majority of congruent $LiNbO_3$ samples, where the Fermi energy is within the lower part of the electronic band gap, V_{Li}^{-1} and Nb_{Li}^{4+} will be the dominant defect centers. V_{Nb}^{-5} may occur in strongly n-type samples, though.

We note that the finite-size and local potential corrections to the DFEs of the defect centers investigated in this work are opposite in sign and compensate each other to a certain extent. This suggests that results obtained within local DFT with finite-size cells profit from some fortuitus error compensation.

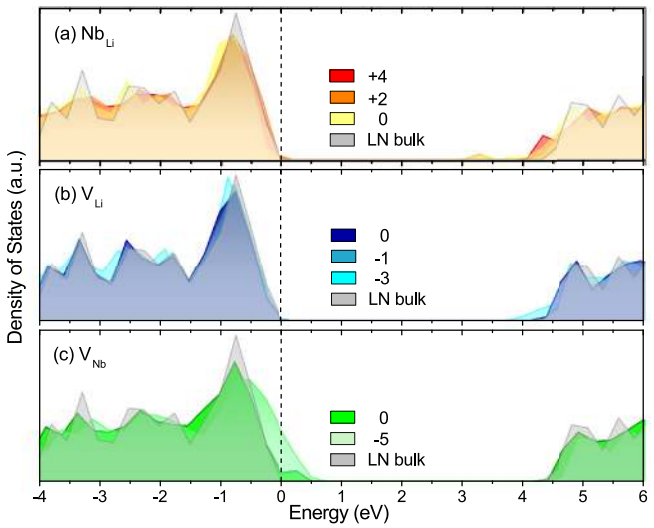

FIG. 7. (Color online) HSE total density of states (arbitrary units) for stable charge states of Nb_{Li}, V_{Li}, and V_{Nb} as well as defect-free LN.

D. Electronic structure

In order to better understand the defect electronic properties, we have calculated the total electronic density of states (DOS) and the electronic charge distribution for the stable charge states of Nb_{Li}, V_{Li}, and V_{Nb} within hybrid DFT (see Fig. 7 and Fig. 8, respectively). Thereby, we plot the difference,

$$\rho(\mathbf{r}) = \rho(X^q,\mathbf{r}) - \rho(\text{bulk},\mathbf{r}) - \sum_i n_i \rho_i(\mathbf{r}), \qquad (6)$$

in order to highlight the charge redistribution upon defect formation. Here $\rho(X^q,\mathbf{r})$ is the total charge density of the cell with the defect X in the charge state q, $\rho(\text{bulk},\mathbf{r})$ is the total charge density of a corresponding bulk supercell, n_i is the number of atoms of species i that have been added to ($n_i > 0$) or removed from ($n_i < 0$) the supercell when the

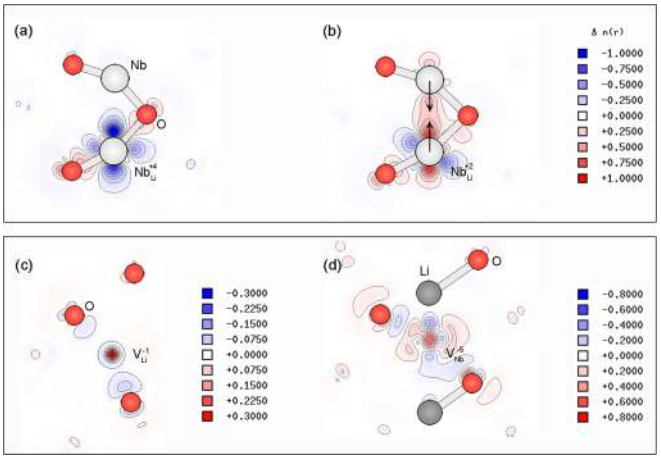

FIG. 8. (Color online) HSE electron density difference for stable charge states of Nb_{Li}, V_{Li}, and V_{Nb} along a $(2\bar{1}\bar{1}0)$ plane. Atomic color coding as in Fig. 1. Blue and red regions represent electron depletion and accumulation, respectively.

defects are created, and $\rho_i(\mathbf{r})$ represents their atomic charge distribution.

The antisite Nb_{Li} is found to be stable in the charge states +4 ($4d^0$), +2 ($4d^2$), and 0 ($4d^4$). While the transition (4+/2+) occurs at midgap and is of crucial importance to understanding the behavior of congruent LN [9,15], the (2+/0) transition occurs only for values of the Fermi energy close to the VBM, where the antisites are energetically unfavorable. Three empty shallow defect states close to the CBM are observed for Nb_{Li}^{+4}, reminiscent of the d^0 electron configuration. One of them is located 0.18 eV below the CBM, and two at degenerate electronic levels 0.06 eV below the CBM. As shown in Fig. 8(a), the defect state charge is strongly localized at the antisite. With rising Fermi level position, this state captures not a single electron, but two electrons simultaneously (negative-U behavior), resulting in the Nb_{Li}^{+2} charge state ($4d^2$). The now occupied defect level downshifts by 1.28 eV in midgap position. Thereby the defect complex experiences a major lattice relaxation, characteristic for negative-U systems. As shown in Fig. 8(b), the nearest Nb atom along the [0001] polarization direction moves toward the Nb_{Li}^{+2} defect by 0.34 Å and forms a covalent bond. In this charge state the antisite can be interpreted as a $Nb_{Li}^{+3}(4d^1)$-$Nb_{Nb}^{+4}(4d^1)$ defect pair. In turn, this defect complex can be interpreted as a bipolaron, i.e., the coupling of a neighboring small bound and a small free polaron [9]. Our hybrid DFT models are in quantitative agreement with LDA + U calculations by Nahm and Park [15]. For $E_F > 4.35$ eV, another two electrons are captured simultaneously, forming two occupied Nb 4d defect states close to the CBM. Also, in this case there is a strong interaction between the Nb antisite and the nearest Nb atom in the [0001] direction.

The Li vacancy V_{Li}^{-1} is characterized by an almost VBM resonant defect state. Thereby the charge density localizes at the O atoms around the Li vacancy. This configuration is stable for a large range of Fermi energies. For $E_F > 4.40$ eV, two electrons are captured simultaneously by the empty d orbitals of the neighboring Nb atoms. A rather delocalized electron state about 0.3 eV below the CBM is formed [cf. Figs. 7(b) and 8(c)]. The (−/3−) transition occurs for high values of the Fermi energy, thus the Li vacancy is expected to be formed only in the singly negative charge state in the vast majority of the LN samples.

The Nb vacancy V_{Nb}^{-5} leads to five defect states that are energetically about 0.52 eV above the VBM, with a large defect-induced charge redistribution mainly localized around the defect and its surrounding O atoms. This defect practically exists only in the −5 charge state, as the other stable charge state, i.e., the neutral state, is energetically strongly unfavorable with respect to other defect centers. The formation of the defect is accompanied by a sizable structural relaxation and rearrangement of the Nb 4d states which build up the VBM. The description of these conduction states is largely improved within hybrid functionals, which explains the pronounced dependence of the V_{Nb} on the XC formulation.

IV. CONCLUSIONS

In conclusion, the stability and electronic structures of Nb_{Li}, V_{Li}, and V_{Nb} point defects in LN have been investigated using hybrid DFT. Extrapolation of the defect formation energies calculated for different-sized unit cells to infinite dimensions allows for the correction of finite-size errors within PBCs. The inclusion of nonlocal Hartree-Fock exchange provides a value for the LN band gap much closer to the value calculated at higher levels of approximation. It also leads to modifications of the point defect energies and the CTLs. The stability of Nb_{Li}^{+4} is enhanced with respect to DFT-PBE simulations. In contrast to earlier findings [16,18], we find V_{Nb}^{-5} more favorable with respect to V_{Li}^{-1} for Fermi levels in the upper half of the band gap. This indicates that for specific conditions Nb vacancies may be formed. These conditions, however, do not correspond to the majority of the samples, where the Fermi energy is in the lower half of the electronic band gap. Thus, the present calculations indicate the coexistence of Nb antisites and Li vacancies in LN, while Nb vacancies may only be formed under particular conditions.

ACKNOWLEDGMENTS

We gratefully acknowledge financial support from the DFG (TRR142 and SCHM1361/21) as well as supercomputer time provided by the HLRS Stuttgart.

[1] G. D. Boyd, K. Nassau, R. C. Miller, W. L. Bond, and A. Savage, Appl. Phys. Lett. **5**, 234 (1964).
[2] F. S. Chen, J. Appl. Phys. **40**, 3389 (1969).
[3] V. Gopalan, V. Dierolf, and D. A. Scrymgeour, Annu. Rev. Mater. Res. **37**, 449 (2007).
[4] F. P. Safaryan, R. S. Feigelson, and A. M. Petrosyan, J. Appl. Phys. **85**, 8079 (1999).
[5] J. G. Bergman, A. Ashkin, A. A. Ballman, J. M. Dziedzic, H. J. Levinstein, and R. G. Smith, Appl. Phys. Lett. **12**, 92 (1968).
[6] E. H. Turner, F. R. Nash, and P. M. Bridenbaugh, J. Appl. Phys. **41**, 5278 (1970).
[7] F. Luedtke, K. Buse, and B. Sturman, Phys. Rev. Lett **109**, 026603 (2012).
[8] A. Riefer, S. Sanna, A. Schindlmayr, and W. G. Schmidt, Phys. Rev. B **87**, 195208 (2013).
[9] O. F. Schirmer, M. Imlau, C. Merschjann, and B. Schoke, J. Phys.: Condens Matter **21**, 123201 (2009).
[10] D. M. Smyth, Prog. Solid State Chem. **15**, 145 (1984).
[11] S. C. Abrahams and P. Marsh, Acta Crystallogr. Sect. B **42**, 61 (1986).
[12] H. Donnerberg, S. M. Tomlinson, C. R. A. Catlow, and O. F. Schirmer, Phys. Rev. B **40**, 11909 (1989).
[13] N. Iyi, K. Kitamura, F. Izumi, J. K. Yamamoto, T. Hayashi, H. Asano, and S. Kimura, J. Solid State Chem. **101**, 340 (1992).
[14] H. Donnerberg, S. M. Tomlinson, C. R. A. Catlow, and O. F. Schirmer, Phys. Rev. B **44**, 4877 (1991).
[15] H. H. Nahm and C. H. Park, Phys. Rev. B **78** 184108 (2008).
[16] H. Xu, D. Lee, J. He, S. B. Sinnott, V. Gopalan, V. Dierolf, and S. R. Phillpot, Phys. Rev. B **78**, 174103 (2008).

[17] A. P. Wilkinson, A. K. Cheetham, and R. H. Jarman, J. Appl. Phys. **74**, 3080 (1993).
[18] Q. K. Li, B. Wang, C. H. Woo, H. Wang, and R. Wang, J. Phys. Chem. Solid **68**, 1336 (2007).
[19] P. A. Schultz, Phys. Rev. Lett. **84**, 1942 (2000).
[20] H. P. Komsa, T. T. Rantala, and A. Pasquarello, Phys. Rev. B **86**, 045112 (2012).
[21] M. Leslie and M. J. Gillan, J. Phys. C: Solid State Phys. **18**, 973 (1985).
[22] G. Makov and M. C. Payne, Phys. Rev. B **51**, 4014 (1995).
[23] S. Lany and A. Zunger, Phys. Rev. B **78**, 235104 (2008).
[24] C. Freysoldt, J. Neugebauer, and C. G. Van de Walle, Phys. Rev. Lett. **102**, 016402 (2009).
[25] F. Bechstedt, *Quasiparticle Corrections for Energy Saps in Semiconductors. Advances in Solid State Physics, Vol. 32* (Springer, Berlin, 1992).
[26] A. Alkauskas and A. Pasquarello, Phys. Rev. B **84**, 125206 (2011).
[27] L. S. dos Santos, W. G. Schmidt, and E. Rauls, Phys. Rev. B **84**, 115201 (2011).
[28] M. Veithen and P. Ghosez, Phys. Rev. B **65**, 214302 (2002).
[29] A. Dhar and A. Mansingh, J. Appl. Phys. **68**, 5804 (1990).
[30] W. G. Schmidt, M. Albrecht, S. Wippermann, S. Blankenburg, E. Rauls, F. Fuchs, C. Rödl, J. Furthmüller, and A. Hermann, Phys. Rev. B **77**, 035106 (2008).
[31] J. Heyd, G. E. Scuseria, and M. Ernzerhof, J. Chem. Phys. **118**, 8207 (2003).
[32] A. V. Krukau, O. A. Vydrov, A. F. Izmaylov, and G. E. Scuseria, J. Chem. Phys. **125**, 224106 (2006).
[33] A. Alkauskas, P. Broqvist, and A. Pasquarello, Phys. Status Solidi B **248**, 775 (2011).
[34] F. Oba, A. Togo, I. Tanaka, J. Paier, and G. Kresse, Phys. Rev. B **77**, 245202 (2008).
[35] P. Deák, B. Aradi, T. Frauenheim, E. Janzén, and A. Gali, Phys. Rev. B **81**, 153203 (2010).
[36] J. L. Lyons, A. Janotti, and C. G. Van de Walle, Phys. Rev. Lett. **108**, 156403 (2012).
[37] A. Janotti and C. G. Van de Walle, Phys. Status Solidi B **248**, 799 (2011).
[38] J. Paier, M. Marsman, K. Hummer, G. Kresse, I. C. Gerber, and J. G. Angyan, J. Chem. Phys. **124**, 154709 (2006).
[39] P. Agoston, K. Albe, R. M. Nieminen, and M. J. Puska, Phys. Rev. Lett. **103**, 245501 (2009).
[40] T. Shimada, T. Ueda, J. Wang, and T. Kitamura, Phys. Rev. B **87**, 174111 (2013).
[41] G. Kresse and J. Furthmuller, Comput. Mater. Sci. **6**, 15 (1996).
[42] G. Kresse and J. Furthmuller, Phys. Rev. B **54**, 11169 (1996).
[43] G. Kresse and D. Joubert, Phys. Rev. B **59**, 1758 (1999).
[44] J. P. Perdew, K. Burke, and M. Ernzerhof, Phys. Rev. Lett. **77**, 3865 (1996).
[45] H. J. Monkhorst and J. D. Pack, Phys. Rev. B **13**, 5188 (1976).
[46] G. C. Van de Walle and J. Neugebauer, J. Appl. Phys. **95**, 3851 (2004).
[47] S. Sanna and W. G. Schmidt, Phys. Rev. B **81**, 214116 (2010).
[48] S. C. Abrahams, J. M. Reddy, and J. L. Bernstein, J. Phys. Chem. Solids **27**, 997 (1966).
[49] U. Gerstmann, P. Dek, R. Rurali, B. Aradi, T. Frauenheim, and H. Overhof, Physica B: Condensed Matter **340-342**, 190 (2003).
[50] A. Savage, J. Appl. Phys. **37**, 3071 (1966).
[51] U. Gerstmann, E. Rauls, H. Overhof, and T. Frauenheim, Phys. Rev. B **65**, 195201 (2002).
[52] P. Lerner, C. Legras, and J. P. Dumas, J. Cryst. Growth **3**, 231 (1968).
[53] G. E. Peterson and A. Carnevale, J. Chem. Phys. **56**, 4848 (1972).